

Geophysical Research Letters

Supporting Information for

High and dry: billion-year trends in the aridity of river-forming climates on Mars

Edwin S. Kite¹, Axel Noblet²

¹University of Chicago, Chicago, IL, USA.

² Nantes Université, Nantes, France.

Corresponding author: Edwin Kite (kite@uchicago.edu)

Contents of this file

Text S1

Figures S1 to S10

Tables S1 to S6

Introduction

Text S1 includes extended description of data and full details of statistical models.

Figures S1 to S8 include HiRISE DTM images (Figures S1 to S4) and extended description of data (Figures S5 to S10).

Tables S1 to S6 include extended description of data. Tables S2, S3, and S5 are each more than one page long, and so per AGU instructions are uploaded as separate files.

Text S1.

Trend of X_H with crater size disfavors brief wet events.

Bigger craters were not any drier than small craters (there is a trend to bigger craters being wetter, $p < 10^{-4}$, with $X_H < 10$ found mainly in large craters, $p = 0.003$) (Fig. 4c). This argues against brief wet events, for the following reason. Let the energetic upper limit on evaporation E be E_{max} . For a given lake, if we have lake area A , drainage area D , and a terrain model, we know the minimum total runoff production P_{tot} in order to flood area A . If the wet event was very brief (short timescale τ), then $P_{tot}/\tau \gg E_{max}$. But if $P_{tot}/\tau \gg E_{max}$, then during a wet event, small craters would fill up more than big craters. So, brief wet climates predict higher X_H for bigger craters ($X_H \propto R_{crater}^{2/3}$) because small sinks fill quicker than big sinks. That is in contradiction to the observations. For fiducial values of $E_{max} = 1$ m/yr (Irwin et al. 2015) and $P_{tot} = 30$ m, each wet event must have lasted at least decades. This disfavors the scenario in which late-stage river-forming climates were powered by the greenhouse forcing from a single volcanic eruption, or the energy of a distant impact.

An alternative way of reaching the same result is as follows. Approximate a lake with volume V as an inverted cone, $V = \frac{1}{3} \pi R_{lake}^2 h$, where h is lake depth. Suppose that crater floors have the same floor slope s , so $V = \frac{1}{3} s \pi R_{lake}^3$. Considering a range of craters with different sizes, for uniform runoff production $V \propto R_{crater}^2$. Thus $R_{lake} \propto R_{crater}^{2/3} \rightarrow (R_{lake}/R_{crater}) \propto R_{crater}^{-1/3}$. Since for a closed basin $X_H \propto (R_{lake}/R_{crater})^2$, $X_H \propto R_{crater}^{2/3}$. Contrary to this prediction, X_H is negatively correlated with R_{crater} (Fig. 4c). This disfavors the brief-wet-event hypothesis. However, brief impact-triggered runoff appears to have occurred at some locations, such as Mojave crater (Goddard et al. 2014). Future work might use variable timescales, and full CTX DTM terrain models, to evaluate allowed combinations of timescale and X_H (Stucky de Quay et al. 2020).

Details of analysis.

To check if the X_H trends could be a statistical artifact, we used two approaches. First, we counted the number of hard constraints falling into rectangular regions in Fig. 4 (bold numbers in Fig. 4). We define a hard constraint to exclude channel-stops, candidate lake deposits, and basins where data permit X_H on both sides of $X_H = 10$. (This is conservative in that channel-stops are probably good paleohydrologic constraints). This leaves 46 data points. The data are not evenly distributed between the rectangular regions. To find the probability that the trends result from chance, we resampled-with-replacement from the hard-constraint occurrences. Resampling showed $p = 0.0017$ for the latitude trend (lower X_H at latitudes S of 10° S), $p = 0.0034$ for the crater-diameter trend (lower X_H for crater diameter > 60 km), and $p = 0.0134$ for the elevation trend (lower X_H at elevations < -1500 m). As an alternative approach to uncertainty quantification, we randomly sampled aridities from a log-uniform prior on $X_H = \{0.1, 10^4\}$, clipped on a per-basin basis to satisfy the geologic constraints. (We did not resample basin occurrence in this approach, only the uncertainty on X_H within each basin). This approach uses all 223 measurements and 118 basins. For each bootstrapped ensemble of basin aridities, we calculated the number of bootstrapped data falling into the rectangular regions shown in Fig. 4. Then, as for the first approach, we assessed trend agreement. From 10^4 bootstraps, we found that in all cases the latitudinal trend is recovered, in all cases the crater-diameter trend is recovered, and in 9422 cases the elevation trend is recovered. We did a sensitivity test using a different log-uniform prior, $X_H = \{0.1, 10^{14}\}$. The sensitivity test results were unchanged for the latitude trend and crater-diameter trend and increased to 9695/10000 for the elevation trend. We conclude that systematic errors are more important than random error in our analysis.

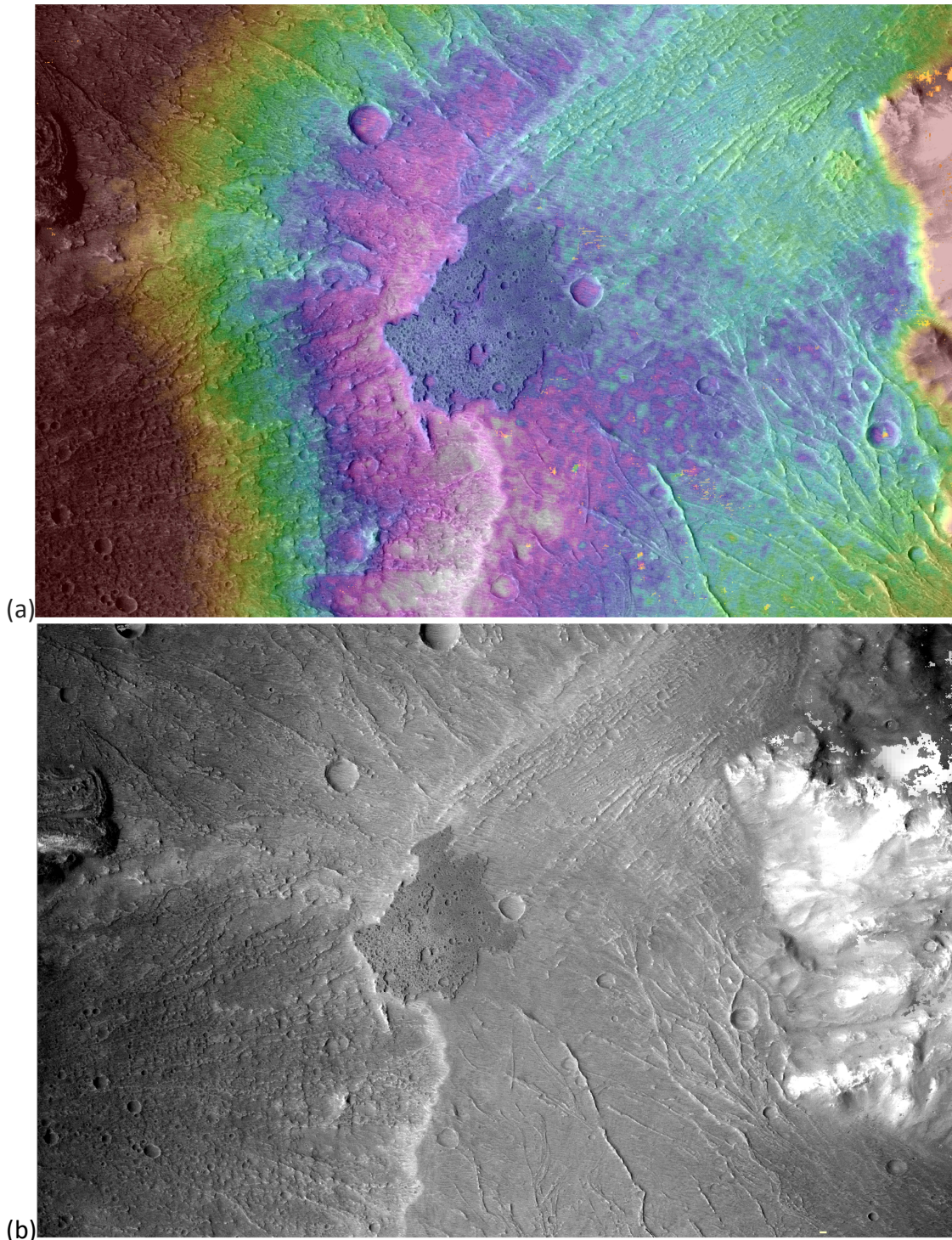
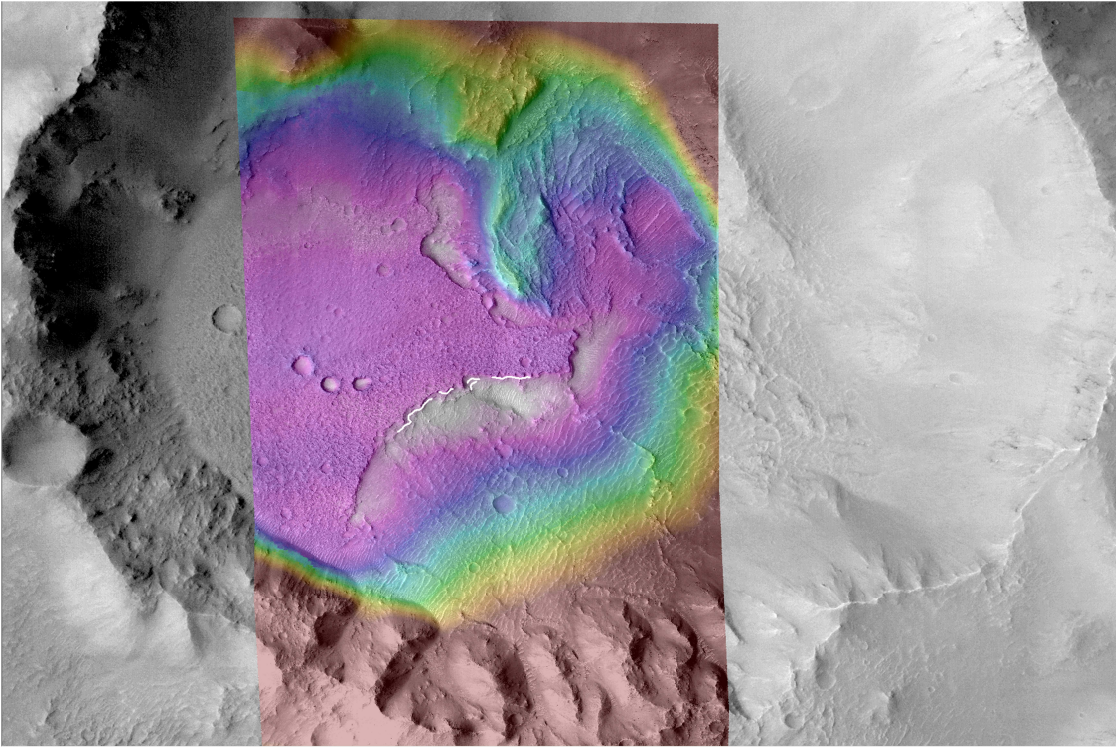
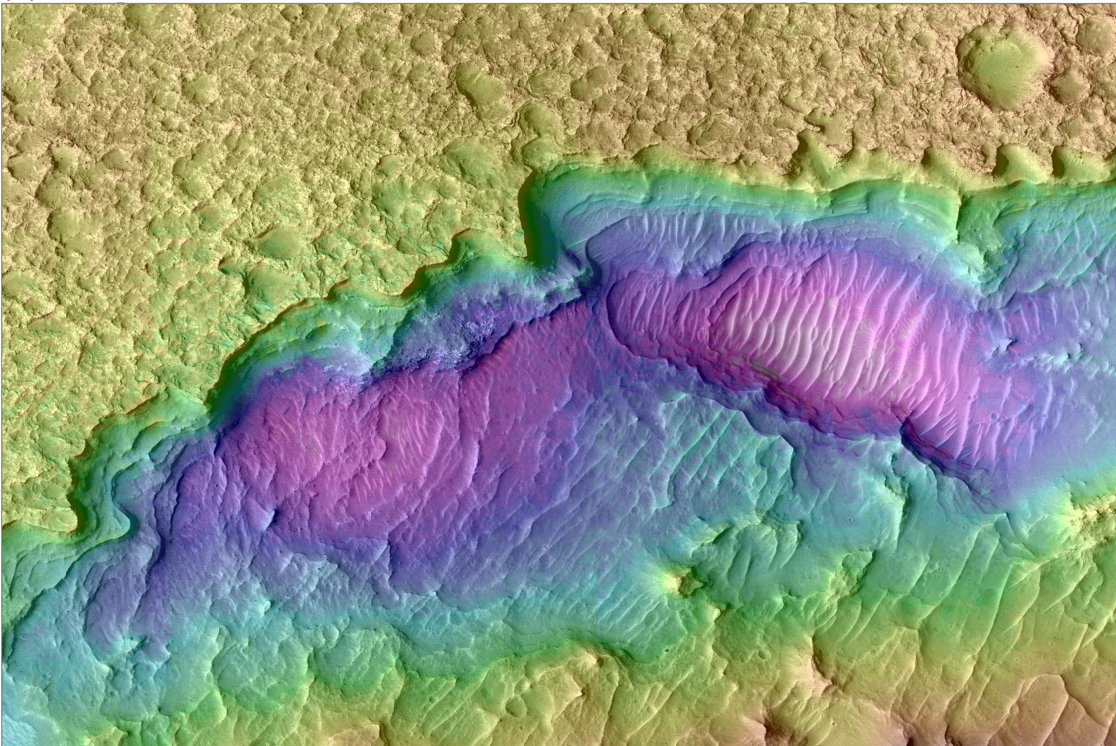


Fig. S1. (a) Example of flat crater-bottom deposit interpreted as a lake/playa deposit - mesa at terminus of wind-eroded alluvial fan deposits. 23°S 74°E. Image is 16.8 km across. Colors highlight elevation range between -1200m (red) and -1350m (white). CTX DTM (stereopair: F10_039889_1567_XN_23S286W and F12_040522_1566_XN_23S286W). **(b)** As (a), but without color elevation overlay.

(a)



(b)



(c)

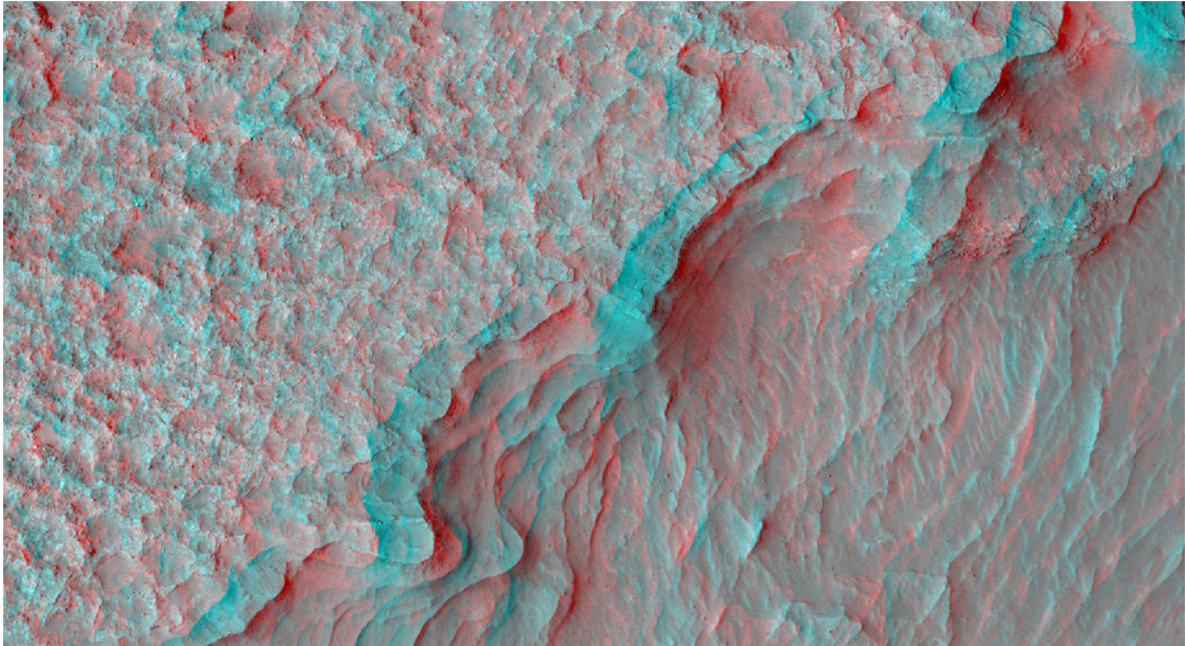
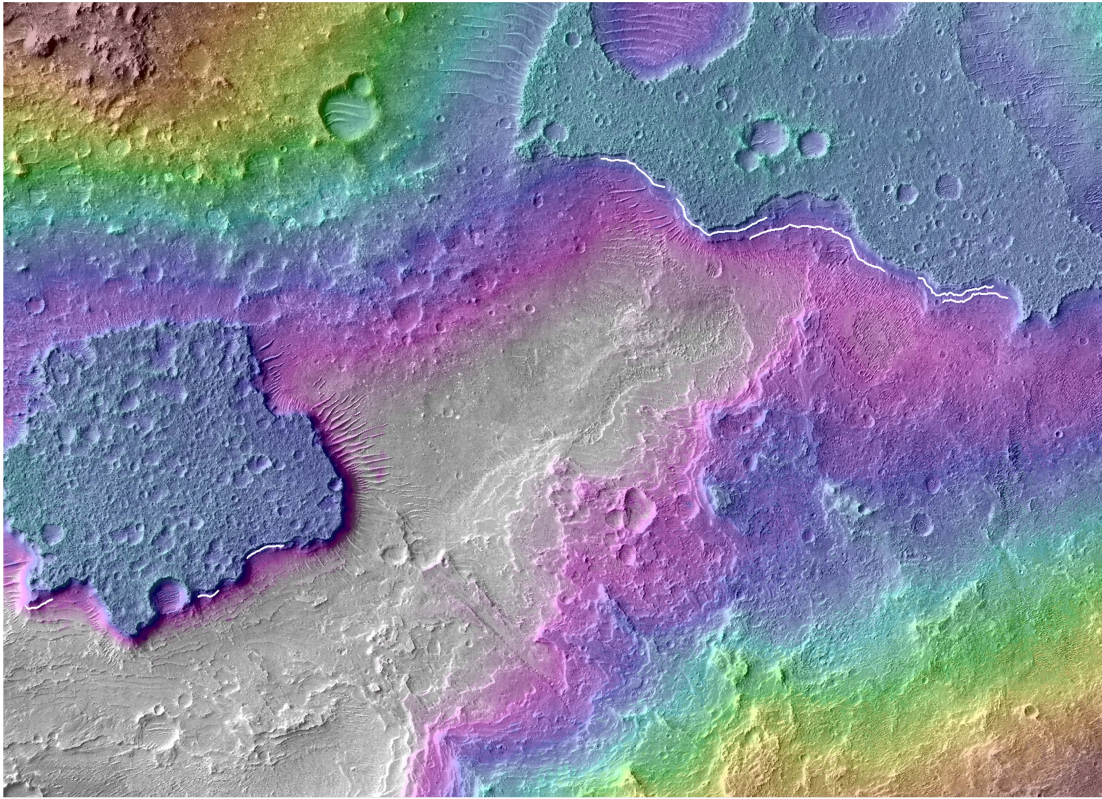
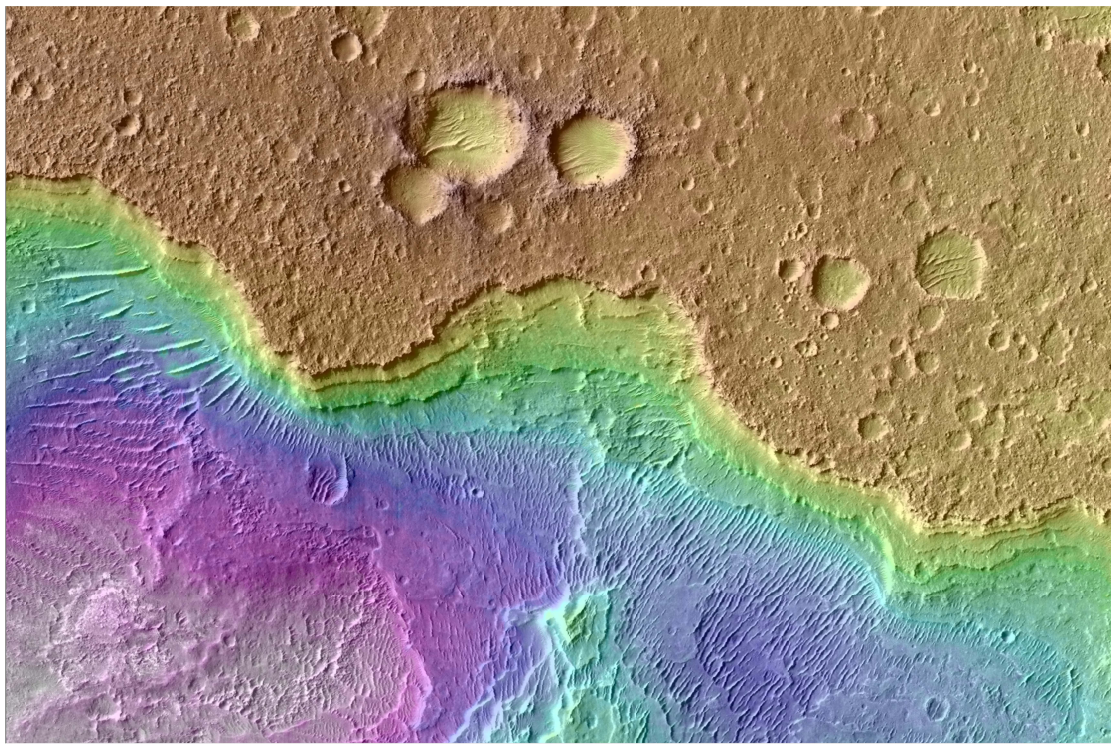


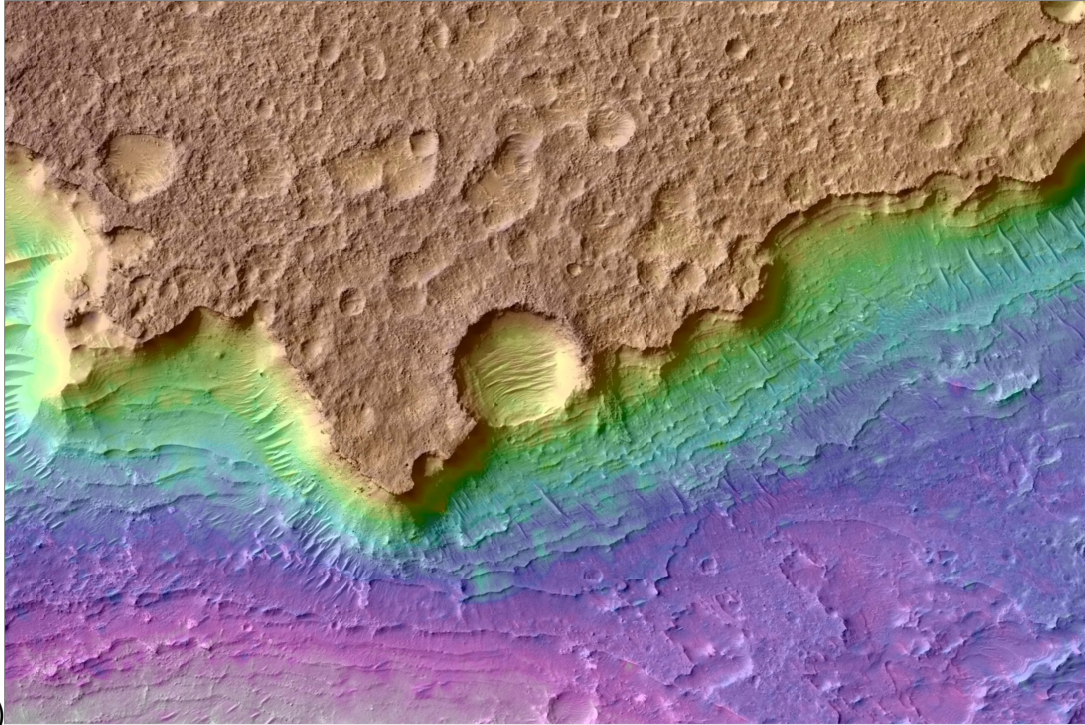
Fig. S2. Additional example of flat crater-bottom deposit interpreted as a playa/lake deposit (30°S 187°E). **(a)** Colored HiRISE DTM (ESP_065414_1495/ESP_065480_1495 stereopair) is 5.2 km across; grayscale background is CTX image. Colors highlight elevation range between 500 m (red) and 300m (white). The flat crater-bottom deposit is the purple mesa in the left center of the DTM. Note erosional alcoves in the S rim of the impact crater, and depositional ramp linking these alcoves to the flat-crater bottom deposit. The depositional ramp is topped by sinuous ridges, one of which feeds into the flat crater-bottom deposit. White lines trace layers whose elevation and orientation were measured (Fig. S8). **(b)** Close-up of the layered scarp corresponding to the white lines in panel (a). Image is 1.6 km across. Colors highlight elevation range between 348m (red) and 284m (white). **(c)** Red-blue anaglyph of the area in the left of panel (a). Image is 920m across. Nearly-horizontal mid-toned layers are exposed beneath the lighter-toned erosionally-resistant cap.



(a)



(b)



(c)

Fig. S3. Additional example of flat crater-bottom deposits interpreted as playa/lake deposits (18°S 323°E, Luba crater). **(a)** Image is 4.9 km across; colors highlight elevation range from -650m (red) to -750m (white) (ESP_072479_1615/ESP_072545_1615 stereopair). Note the alluvial fan deposit extending down from the bottom right. The white lines trace layers whose elevation and orientation were measured (Fig. S8). **(b)** Close-up of the area corresponding to the right cluster of white lines in panel (a). Image is 1.85 km across. Colors highlight elevation range between -705 m and -751 m. **(c)** Close-up of the area corresponding to the left cluster of white lines in panel (a). Image is 1.5 km across. Colors highlight elevation range between -707 m (red) to -779 m (white).

76

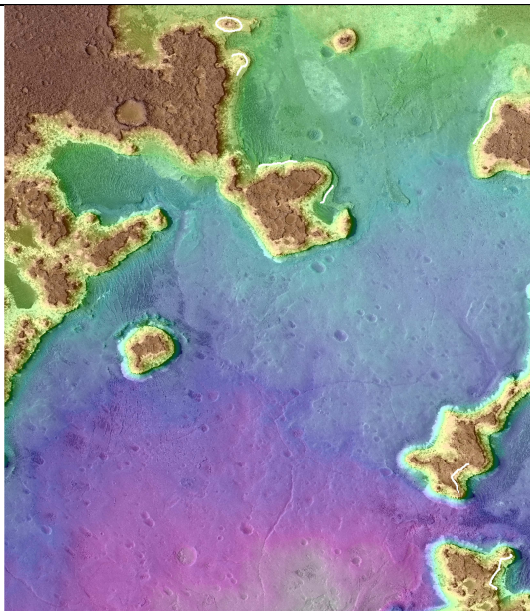


Fig. S4. Additional example of flat crater-bottom deposit interpreted as a playa/lake deposit (PSP_003526_1510/PSP_003249_1510 stereopair, -29°S 309°E, Ritchey crater). Image is 5.9 km across. Colors highlight elevation range between -1355m (red) and -1551m (white). White lines indicate layer traces.

77

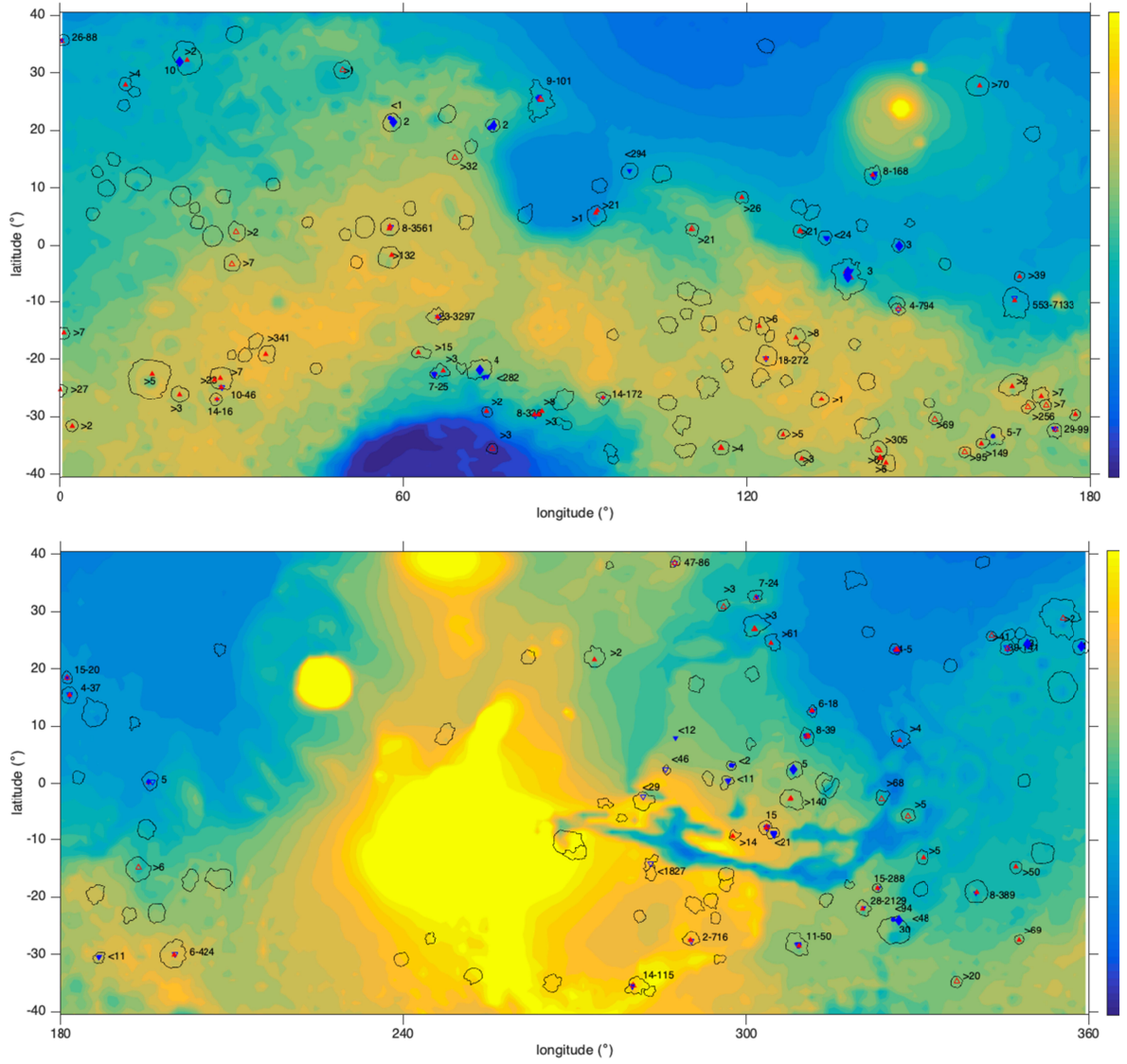


Fig. S5. Detailed version of Fig. 2a, showing X_H constraints for different basins. Black contours locate young impact craters (“AHi” units from Tanaka et al. 2014) inspected for paleohydrology constraints. Blue triangles = flat crater-bottom deposits (interpreted as lake deposits) (unfilled = candidate), blue diamonds = deltas/shorelines, blue circles = internal spillways, red filled triangles = alluvial fan toes, red unfilled triangles = channel-stops. There is scatter in X_H between nearby craters. Among other possibilities, the variability might be caused by lithological control (e.g., varying infiltration losses due to varying saturation hydraulic conductivity), the effect of crater shape on local meteorology (Steele et al. 2018), or feedback between erosion and snowmelt runoff (e.g., amplifying small differences in slope).

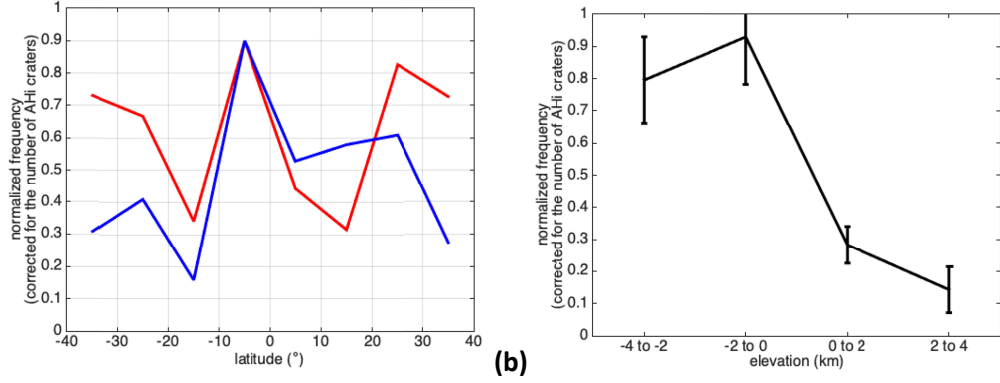


Fig. S6. (a) Detailed break-out of Fig. 2b, showing distribution with latitude of craters containing (blue line) geomorphic evidence for lower limits on lake extent and (red line) geomorphic evidence for upper limits on lake extent. **(b)** Distribution of frequency of craters with paleohydrologic evidence with elevation. Vertical bars correspond to \sqrt{N} uncertainty. Numbers correspond to per-bin sample size.

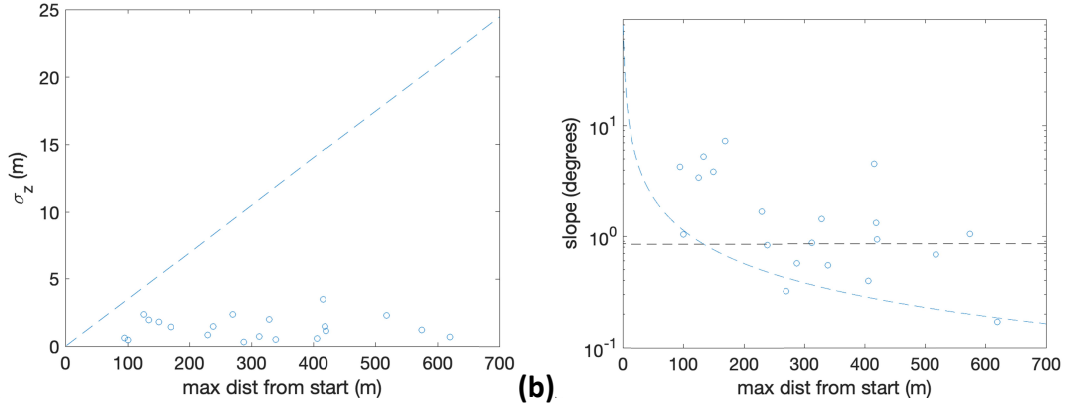


Fig. S7. Properties of layers within flat crater-bottom deposits interpreted as lake deposits. (a) The standard deviation of elevation of points along the trace is consistent with flat, taking into account tracing error and DTM uncertainty. **(b)** The median best-fit dip for traces >200 m long (black dashed line) is $<1^\circ$, consistent with flat taking into account tracing error and DTM uncertainty. Orientations were calculated using the method of Lewis et al. (2008).

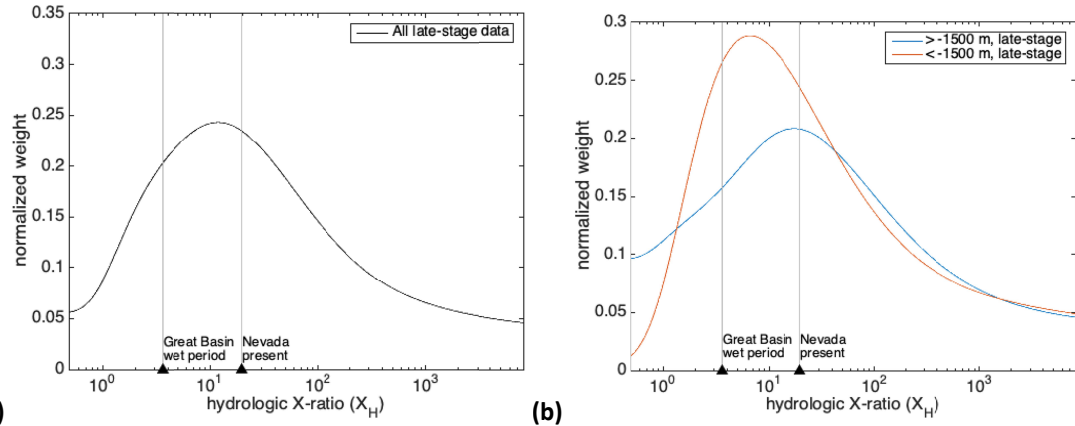


Fig. S8. Sensitivity test for Fig. 3, to show the effect of choosing a different log-uniform prior on X_H , specifically $\{0.1, 10^{14}\}$. Modern-Earth aridity values shown by black triangles are from Matsubara et al. (2011). (a) Overall late-stage aridity. **(b)** Kernel density estimate of late-stage X_H changes with elevation.

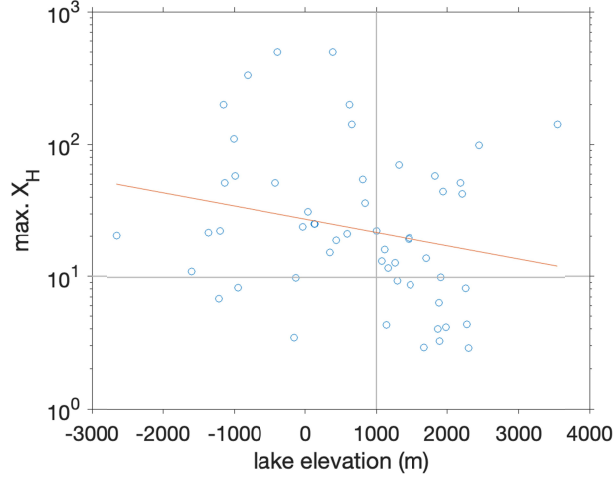


Fig. S9. Evidence for high-and-wet early stage dependence of aridity index on elevation. Upper limits on early-stage X_H (high X_H corresponds to greater aridity) from lake overflows using the data of Stucky de Quay et al. (2020). Paleolake locations from Table S1 in Stucky de Quay et al. (2020) Table S1 ($n = 54$) were interpolated in 8 pixels-per-degree MOLA data to obtain elevations. (Note that the larger and less selective dataset of Fassett & Head 2008 shows a weaker trend, with the same sign). The gray lines highlight the paucity of $X_H < 10$ constraints at elevations below +1000 m, and the red line corresponds to the least-squares best fit. The median X_H lake-overflow bound above +1 km is $X_H < 12$, and the median X_H lake-overflow bound above +1 km is $X_H < 25$.

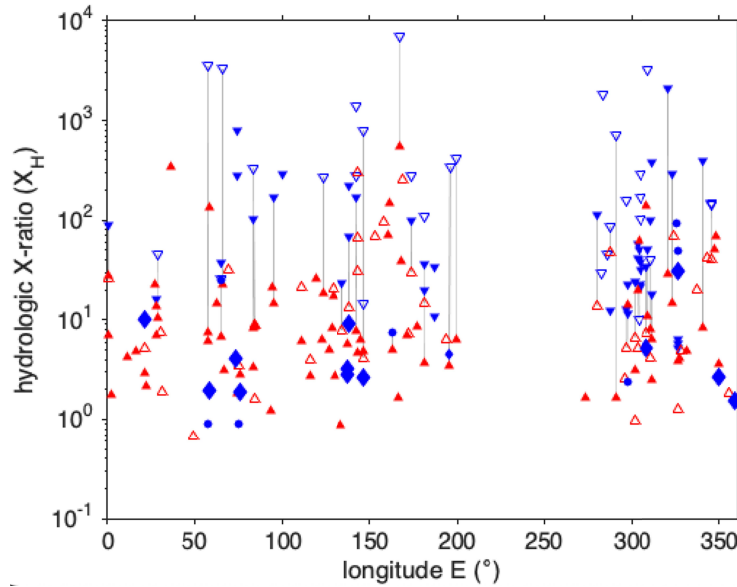


Fig. S10. Late-stage aridity constraints versus longitude (supplements Fig. 4). Blue triangles are upper limits on aridity (e.g. lake deposit extent), red triangles are lower limits on aridity, (e.g. from alluvial fan termini), and blue diamonds are best-estimates of lake elevation (e.g., from a delta top). Blue triangles=flat crater-bottom deposits (interpreted as lake deposits) (unfilled=candidate), blue diamonds = deltas/ shorelines, blue circles=internal spillways, red filled triangles=alluvial fan toes, and red unfilled triangles=channel-stops. Numbers correspond to the number of constraints lying entirely inside a rectangular region. Gray lines connect lowest and highest constraints for a single basin. The gap in longitude corresponds to the high, young volcanic province Tharsis.

<i>Location</i>	<i>Evidence (pre-fluviolacustrine-sed or syn-fluviolacustrine-sed impact craters internal to AHi impact rims) (ϕ = diameter)</i>	<i>Main-crater diam. (km)</i>	<i>Estimate [*] of Time Gap</i>
83°E 30°S (Nako)	Rivers/lakes activity postdate ejecta from large crater (40 km diameter?) to the E → long time gap	43	At least Gyr
167°E 10°S (Reuyl)	ϕ = 6 km crater on SW side contains fan.	86	0.4 Gyr
303.5°E 7.6°S	ϕ = 2 km crater inside large crater (on W side) has inlet breach or alcove.	45	0.2 Gyr
311°E 8°N	Contains ϕ = 11 km crater that has alcoves, fans, and a possible lake deposit. [**]	68	0.2 Gyr
326°E 23°N (Wahoo)	Material with lineations perpendicular to high relief grades into wind-eroded material that is itself embayed by smoother, ramp material with much less wind erosion. Channel also postdates wind erosion.	67	At least Myr (to allow time for wind erosion)
84°E 25.4°N (Peridier)	ϕ = 9 km crater on NW side is prefluvial.	100	0.6 Gyr
22°E 32°N (Cerulli)	Channel crosscuts ϕ = 7 km crater on the SW rim.	130	0.2 Gyr
144°E 38°S	Exit breach on ϕ = 2km crater on E side (internal to main crater).	47	0.2 Gyr
187°E 30°S	FCBD postdates ejecta from ϕ = 10 km crater on E rim (which itself contains an FCBD).	31	6.5 Gyr (sic)
297.5°E 3°N	Inlaid ϕ = 4 km crater inside W rim has exit breach into main crater.	27	2 Gyr
280°E 36°S	Probable exit-breach crater (ϕ = 6 km), inside N rim.	69	0.6 Gyr
326°E 26°S (Holden)	Noted by Irwin et al. (2015) and Kite et al. (2017).	154	At least Myr
Kite et al. 2017 sites (14 craters)	Interbedded craters. See Kite et al. 2017.	Varies between sites.	>(100–300) Myr

Table S1. Evidence against a localized impact trigger for late-stage rivers and lakes. Notes: [*] Best-estimate time gap assuming modern impact flux (valid for the Amazonian, too low by a factor of 3.2 at 3.5 Ga) and the Hartmann chronology, using the nearest bin in the tables of Michael (2013). Assuming the count area for detection of interbedded craters is the entire crater (which will greatly understate the true time gap), and dividing results by a factor of 20 to take account of the fact that we only found interbedded craters in 12 of the ~219 craters that we surveyed. In reality synsedimentary and presedimentary impact craters are usually detected at/near the perimeter of sedimentary deposits, so the survey area is smaller than assumed here. Thus these estimates are crude and are likely biased low; even so, the timescales are long. [**] Additionally, PSP_008167_1885 shows a 700m-diameter crater prograded into by, and so predating, the Tyras fan. In addition to the craters tabulated here, sediments of uncertain origin (plausibly lacustrine) postdate a 1km-diameter crater within the SE of the 37km-diameter fan-bearing crater at 174°E 32°S.

Table S2. Constrained basins. [Table uploaded separately per AGU instructions] Explanation. A zero or dash corresponds to “no constraint.” Constraint types: 1 = Fan terminus. 2 = Channel terminus. 3 = Delta break-in-slope elevation or stepped-delta top. 4 = Fan toe/playa contact. 5 = Lake deposit. 7 = Candidate lake deposit. 10 = Overspilled contour. 11 = Shoreline feature. Additional notes. At Gale crater, we adopted Palucis et al. (2016)’s interpretation that the Pancake Delta is post-Mt. Sharp, fed by a small enclosed-basin catchment. The elevation of candidate shoreline features inside Nicholson crater (Salese et al. 2019; ESP_059361_1795) were treated as a best estimate of past lake level (a blue diamond in Fig. 4). At Saheki crater (Morgan et al. 2014), we observed the transition between an alluvial fan and a playa deposit. The elevation contour corresponding to this transition corresponds to our best-estimate of paleolake extent (a blue diamond in Fig. 4). Our approach treats the present-day topographic relationships between lake deposit outcrops and alluvial fan deposit outcrops as being representative of the topographic relationships between deposits when the rivers were flowing. Sometimes we observe FCBDs topographically above fan toes (e.g., at Luba crater), presumably due to differential wind erosion. Holden is omitted as the drainage area at the time deltas formed (Grant et al. 2008) is not known. At Peridier, channels extend topographically below the flat crater-bottom deposits that we interpret as lake deposits, perhaps corresponding to a later wet episode.

Table S3. Fan terminus or delta-top elevation contours. [Table uploaded separately per AGU instructions] Explanation: Constraint types: 1 = Fan terminus. 2 = Channel-stop. 3 = Delta break-in-slope or Stepped-delta top. 4 = Fan terminus/playa intersection.

Lon (°)	Lat (°)	Elev (m)	Lake area at overflow/shoreline (km ²)	Topog. catchment area (km ²)	Hydrologic X-ratio, X_H	Diam. of host crater (km)	Notes
325.83	-23.71	-520	164.23	15540.70	93.63	n.a.	1.
326.58	-23.92	-1400	422.84	20921.80	48.48	62	2.
195.28	0.34	-4420	1423.02	7853.98	4.52	100	3.
297.42	3.18	-100	10.53	36.00	2.42	27	4.
57.75	22.19	945	448.14	855.30	0.91	33	5.
75.07	20.36	-540	440.47	836.00	0.90	33	SW of Hargraves.
163.07	-33.45	-540	221.64	1849.70	7.35	59	
65.33	-22.50	-1885	19.36	502.00	24.93	43	SW of Harris.

Table S4. Overspilled contours + shoreline feature. Notes: 1. Overspilled contour corresponds to a sediment trap upstream of the Eberswalde Delta. Topographic catchment is within the ejecta blanket of Holden crater (151 km diameter). 2. Overspilled contour within Eberswalde crater (Irwin et al. 2015). 3. This corresponds to ridges interpreted as a shoreline feature at Nicholson crater (Salese et al. 2019). 4. A 5×4 km crater-in-crater with an exit breach. 5. Exit-breach 33 km diameter crater immediately adjacent to a 71 km crater.

Table S5. Flat Crater-Bottom Deposits Interpreted as Lake Deposits [Table uploaded separately per AGU instructions] Notes: * When lake deposits were close to one another and appeared to be deposits from the same wet event, we combined their areas for the purpose of assessing lake size. In this table, deposit area is added to subsequent deposit area (with a common same drainage area) to give a combined hydrologic constraint. The area of the individual deposit is the difference between rows.

** Combined lake areas for hydrology constraint.

*** Combined with FCBDs for hydrology constraint.

Name	Stereopair image 1	Stereopair image 2	DTM resolution
Luba1	ESP_072479_1615	ESP_072545_1615	2m
Luba2	ESP_019467_1615	ESP_018966_1615	2m
Ritchey	PSP_003249_1510	PSP_003526_1510	1m
Unnamed_Magelhaens	ESP_065480_1496	ESP_065414_1695	1m

Table S6. HiRISE DTMs made for this study.